Measurements and Modelling of Amorphous and Nanocrystalline Materials up to 1 GHz

Carlo Ragusa[1], Samuel Dobák[2], Cinzia Beatrice[3], Luigi Solimene[1], and Fausto Fiorillo[3]

[1]Department of Energy, Politecnico di Torino, Torino 10129, Italy

[2]Institute of Physics, Faculty of Science, P.J. Šafárik University, 04154 Košice, Slovakia.

[3]Advanced Material Metrology and Life Science Division, Istituto Nazionale di Ricerca Metrologica, Torino 10135, Italy.

Corresponding author: Carlo Ragusa (e-mail: carlo.ragusa@polito.it).

This research was carried out in the framework of the 19ENG06 HEFMAG project, funded by the EMPIR program, and co-financed by the Participating States and the European Union's Horizon 2020 research and innovation program.

ABSTRACT We highlight the challenges posed by the experimental and theoretical assessment of the magnetic losses in magnetic materials for high-frequency applications, with specific reference to amorphous and nano-crystalline magnetic materials. After pointing out the role of magnetic materials in high-frequency applications and problems raised by broadband magnetic characterization, we discuss the physical modeling of magnetic permeability and losses over the whole extended range of frequencies where the magnetic response of the material can be appreciated. The experiments have been performed on field annealed Co-based and nanocrystalline Finemet type ribbons, having thickness ranging between ~13 μm and ~25 μm. The samples under test are endowed with defined transverse magnetic anisotropy. Magnetic losses and complex permeability have been measured from DC to 1 GHz by combined application of fluxmetric and transmission line methods. The remarkable wideband soft magnetic properties of these materials are theoretically assessed by combined solution of Maxwell's and Landau-Lifshitz-Gilbert equations and its consistent incorporation with the concept of loss decomposition.

INDEX TERMS Amorphous magnetic materials, Inductors, Magnetic cores, Magnetic devices, Magnetic losses, Magnetic measurements, Magnetics

I. INTRODUCTION

The soft magnetic materials available to the industry are required to cover a large array of applications, from the classical use as cores of transformers, generators, and motors to a great variety of parts and components displaying magnetic properties and intended for electronics in a wide range of application areas. Such applications nowadays call for soft magnetic materials with high permeability and low losses over a broad range of frequencies, from DC to several MHz [1-4]. The most interesting materials for high-frequency applications are soft ferrites, amorphous, and nano-crystalline alloys, which can display useful soft magnetic behavior upon an extremely wide range of frequencies, up to hundreds of megahertz [5-7]. The sintered ferrite cores are the standard industrial products, with the Ni-Zn types covering a broader frequency range, typically up to 10 MHz versus a typical 1 MHz limit of Mn-Zn ferrites, at the cost of reduced permeability. Amorphous soft magnetic materials are non-crystalline materials that have no magneto-crystalline anisotropy. Interesting soft magnetic properties are found in Iron-based alloys with relatively high saturation magnetic polarization and in Co-based alloys with near-zero magnetostriction. Fig. 1 provides an overview of the magnetic behaviour of nanocrystalline Finemet and Co-based amorphous ribbons, and Mz-Zn sintered ferrites. The latter have relatively low saturation magnetization (J_s = 0.4 – 0.5 T), a limitation that is largely overcome in the nanocrystalline cores (J_s ~ 1.25 T), which additionally display higher permeability and lower losses at all frequencies. These properties weakly depend on temperature, in sharp contrast with the response of the Mn-Zn ferrites, but they come at a higher commercial price.

The investigation of soft magnetic materials for high-frequency applications is generally directed at elucidating and predicting two basic technical parameters: magnetic permeability and energy losses. Under weak fields, the material often displays a quasi-linear magnetic behavior, which can be lumped in a complex permeability. A sinusoidal field elicit a phase-shifted sinusoidal

induction. The complex permeability contains then the information regarding the energy loss. Under high excitation levels, the primary technical parameters are the amplitude permeability $\mu = B_p/(\mu_0 H_p)$, where B_p is the peak induction and H_p is the peak magnetic field, and the specific power loss W. General characterization under controlled sinusoidal and non-sinusoidal induction can be achieved with a fluxmetric setup, an example of which is shown in Fig. 2. It is a standard configuration by which the magnetic properties, the specific power loss and the amplitude permeability are obtained. At high frequencies, spurious phase shifts between the measured primary current and the secondary voltage are minimized by suitable arrangement of the windings and the choice of an anti-inductive shunt resistor R_h [8]. The induction waveform and the field strength in the core are determined by measuring the voltage across the secondary winding and the peak value of the voltage across the resistor R_h. The measurements are carried out at specified values of peak induction, frequency and temperature. The power loss is obtained through the multiplication of the same voltages and their integration over one period. The typical upper-frequency limit of a few MHz, intrinsic to the fluxmetric method, does not permit one to perform, in general, a full permeability and loss analysis up to the frequencies where the magnetic response of the materials becomes negligible. Under these circumstances, a natural solution for high-frequency characterization is provided by a measurement of the sample impedance using a Transmission Line Method (TLM). A setup realizing such an approach is shown in Fig. 3. The complex permeability of a ring sample is obtained here up to a few GHz, using a Vector Network Analyzer (VNA), which feeds a shorted 50-ohm coaxial cable, holding the sample at its bottom. The VNA generates a frequency-swept signal and provides the frequency dependence of the impedance at the sample plane. This can be related, at each frequency, to the geometry of the sample, permitting one to retrieve the complex permeability versus frequency behavior.

In this paper we present experimental results regarding the measurements of magnetic loss and complex permeability on tapewound toroidal samples of amorphous and nanocrystalline ribbons. The characterization has been performed for sinusoidal flux from DC to 1 GHz, using both the fluxmetric and the transmission line methods. The ribbons have been subjected to annealing under transverse saturating magnetic field and exhibit, besides a transverse domain structure, excellent combination of low broadband losses and high permeability. The results are theoretically assessed, across the whole many-decade frequency span, by modeling the frequency dependence of the magnetic loss associated with the rotation of the magnetization, the chief magnetization reversal mechanism in the so-treated materials, by coupling the Maxwell's equations and the Landau-Lifshitz-Gilbert equation. The loss decomposition principle is then applied, permitting one to separately predict the loss contribution by the moving domain walls.

II. EXPERIMENTAL

We measured the magnetic losses and the complex permeability of amorphous and nanocrystalline ribbons from DC to 1 GHz by combined application of fluxmetric and transmission line methods. We analysed two Co-based amorphous ribbons, ~13 μm and ~25 μm tick, and two nanocrystalline Finemet ribbons, ~13 μm and ~20 μm tick, all endowed with defined transverse anisotropy. Tapewound 18 mm diameter ring samples were prepared with 10 mm wide $Fe_{73}Nb_3Cu_1Si_{16}B_7$ precursor amorphous ribbons, obtained by planar flow casting and encased in boron nitride toroidal holders. No tensile stress was applied to the ribbon during winding, the number of layers varying between 3 and 10 from sample to sample. Nanocrystallization annealing, performed at 550 °C, was followed by very slow cooling to room temperature, under a saturating DC field, by which a transverse anisotropy could be induced. The tapewound ring samples of amorphous $Co_{67}Fe_4B_{14.5}Si_{14.5}$ (~13 μm and ~25 μm tick) were subjected to stress-relaxation annealing of two hours at 360°C, followed by two-hour annealing at 280°C and slow cooling under saturating transverse field. In all cases, the transverse applied field strength was $H_\perp$ = ~15 kA/m. The complete datasets are available in [9].

Figure 4. shows an example of wideband characterization of the 13 μm tick Co-based amorphous ribbon. The flux-metric method and the TLM are applied over different overlapping regions of the frequency spectrum. First, the flux metric method is used between DC and a few MHz at given values of the sinusoidal peak induction. Next, the TLM is applied from some 100 kHz up to 1 GHz. In the latter case, the measure is performed under defined exciting power, typically 1 mW or 10 mW. It is observed how the results provided by the two different methods superpose in the shared frequency region. The same conclusion is drawn from Fig. 5, concerning the 20 μm tick Finemet ribbon. This implies, in particular, that the quasi-linear behavior of the material is preserved for J_p = 50 mT, with the measured real μ′ and imaginary μ″ permeability components near-independent of the peak polarization value. Consequently, we can write for the energy loss at a given J_p

$$W_{\mathrm{rot}} = \frac{\pi}{\mu_0} \cdot \frac{(\mu'')_{\mathrm{vna}}}{(|\underline{\mu}|)^2_{\mathrm{vna}}} \cdot B_p^2 \qquad \left[\frac{\mathrm{J}}{\mathrm{m}^3}\right] \tag{1}$$

On the other hand, at low frequencies, the rotational loss is computed through the classical formula, neglecting skin effect,

$$W_{\mathrm{rot}} = \frac{\pi^2}{6}\sigma d^2 f B_{\mathrm{p}}^2. \qquad [\frac{\mathrm{J}}{\mathrm{m}^3}] \qquad (2)$$

An overall view of the loss behavior vs frequency in the same transverse anisotropy Finemet is given in Fig. 6, where J_{p} is made to range between 0.5 mT to 200 mT. Here, the fluxmetric measurements are shown to smoothly superpose, for all J_{p} values, to the TLM results in the overlapping medium frequency range.

III. THEORETICAL ANALYSIS

We treat the case of transversally field-annealed ribbons, where a sharp transverse domain structure is induced by annealing under saturating transverse field (Fig. 7a). Under an oscillating longitudinal applied field, the magnetization process will follow almost completely the mechanism of spin rotation (Fig. 7b). The domain walls that are set in motion by the applied field, through an indirect magnetostatic field, negligibly contribute to the magnetization reversal, but are the source of hysteresis and excess dynamic loss. A theoretical approach to the rotational loss is here applicable because the spin rotation is a homogeneous process that can be naturally associated with a classical loss model with the Maxwell's equations coupled to the constitutive equation of the material. According to the theory, the local behaviour of the material can be represented through a complex susceptibility $\underline{\chi}(j\omega) = \underline{m}_y/\underline{h}_{ey}$, where $\underline{m}_y$ is the magnetization and $\underline{h}_{ey}$ is the effective field. The starting point of this representation is the description of the rotational magnetization process with the Landau-Lifshitz-Gilbert (LLG) equation for the spin dynamics. In the linear approximation, an expression for the complex susceptibility is obtained, under harmonic regime, in the form

$$\frac{1}{\underline{\chi}(j\omega)} = h_0 + j\frac{\omega}{\gamma J_{\mathrm{s}}}\alpha - \frac{\omega^2}{\gamma^2 J_s^2}\frac{1}{(h_0 + N_z + j\,\omega/(\gamma J_{\mathrm{s}})\,\alpha)} \qquad (3)$$

where ω is the angular frequency, J_{s} is the saturation polarization, $\gamma = 1.76 \times 10^{11}$ ($\mathrm{T^{-1}\,s^{-1}}$) is the electron gyromagnetic ratio, α is the damping factor, N_z is the demagnetizing factor along the normal to the ribbon surface, $h_{\mathrm{o}} = 2K\mu_o/J_{\mathrm{s}}^2$ is the reduced anisotropy field $H_{\mathrm{k}}/M_{\mathrm{s}}$, with K ($\mathrm{J/m^3}$) the anisotropy constant. The expression (3) can be written as

$$\underline{\chi}(j\omega) = \frac{\chi_{\mathrm{DC}}}{1 - \frac{\omega^2}{\omega_0^2} + j\frac{\omega}{\omega_1}} \qquad (4)$$

where the DC susceptivity is

$$\chi_{\mathrm{DC}} = 1/h_{\mathrm{o}}, \qquad (5)$$

the resonance angular frequency ω_0 is

$$\omega_0 = \gamma I_s \cdot \sqrt{h_{\mathrm{o}}(h_{\mathrm{o}} + N_{\mathrm{z}})}/\sqrt{1+\alpha^2}, \qquad (6)$$

and the relaxation angular frequency ω_1 is

$$\omega_1 = \gamma I_s/\alpha \cdot h_{\mathrm{o}}(h_{\mathrm{o}} + N_{\mathrm{z}})/(2h_{\mathrm{o}} + N_{\mathrm{z}}). \qquad (7)$$

The electromagnetic analysis is performed by coupling the constitutive equation (4) to the Maxwell's diffusion equation governing the magnetization profile along the thickness in the plate of conductivity σ

$$\frac{\partial^2 \underline{h}_y}{\partial z^2} = j\omega\sigma\underline{b}_y = j\omega\sigma\mu_0\left(\underline{m}_y + \underline{h}_y\right). \qquad (8)$$

Here, $\underline{b}_y = \mu_0\left(\underline{m}_y + \underline{h}_y\right)$ is the flux density, and $-d/2 \le z \le d/2$. Introducing the constitutive equation, we obtain

$$\underline{m}_y = \underline{\chi}(j\omega) \cdot \underline{h}_{ey} = \underline{\chi}(j\omega) \cdot \left(\underline{h}_y + l^2\frac{\partial^2 \underline{m}_y}{\partial z^2}\right) \qquad (9)$$

where the term $l^2 \cdot \partial^2\underline{m}_y/\partial z^2$is the exchange field, $l = \sqrt{2A\mu_o/J_s^2}$ is the exchange length, with A (J/m) the stiffness constant. Given the symmetry of the problem, z can be restricted to $0 \le z \le d/2$. The following boundary conditions apply:

$$\left.\frac{\partial \underline{h}_y}{\partial z}\right|_{z=0} = 0, \qquad (10)$$

and

$$\left.\frac{\partial^3 \underline{h}_y}{\partial z^3}\right|_{z=0} = 0, \qquad (11)$$

because the even symmetry of $\underline{h}_y$;

$$\left.\frac{\partial \underline{h}_y}{\partial z}\right|_{z=d/2} = j\omega\sigma B_{\mathrm{p}}\, d/2, \qquad (12)$$

with B_{p} the average value of the peak induction across the sample thickness.

$$\left.\frac{\partial \underline{m}_y}{\partial z}\right|_{z=d/2} = 0, \tag{13}$$

because a natural Neumann boundary condition holds. From (8) (12) and (13) we obtain

$$\left.\frac{\partial^3 \underline{h}_y}{\partial z^3}\right|_{z=d/2} = j\omega\sigma\mu_0\left(\left.\frac{\partial \underline{h}_y}{\partial z}\right|_{z=d/2} + \left.\frac{\partial \underline{m}_y}{\partial z}\right|_{z=d/2}\right) = -\omega^2\sigma^2\mu_0 B_\mathrm{p}\, d/2. \tag{14}$$

Eliminating $\underline{m}_y$, by replacing (8) in (9), and using (3) we obtain

$$l^2\frac{\partial^4 \underline{h}_y}{\partial z^4} - \left(h_0 + j\frac{\omega}{\gamma J_\mathrm{s}}\alpha - \frac{\omega^2}{\gamma^2 {J_\mathrm{s}}^2(h_0 + N_z + j\,\omega/(\gamma J_\mathrm{s})\,\alpha)} + j\omega\sigma\mu_0 l^2\right)\frac{\partial^2 \underline{h}_y}{\partial z^2} + j\omega\sigma\mu_0\left(1 + h_0 + j\frac{\omega}{\gamma J_\mathrm{s}}\alpha - \frac{\omega^2}{\gamma^2 {J_\mathrm{s}}^2}\right)\underline{h}_y = 0. \tag{15}$$

Equation (15) can be solved analytically together with the boundary conditions (10), (11), (12), (14), providing the magnetic field and the magnetization profile along the thickness. The solution of (15) is

$$\underline{h}_y(z) = C_1\frac{\cosh(\lambda_1 z)}{\sinh(\lambda_1\, d/2)} + C_2\frac{\cosh(\lambda_2 z)}{\sinh(\lambda_2\, d/2)} \tag{16}$$

where λ_1 and λ_2 are the solution of the secular equation

$$l^2\lambda^4 - \left(h_0 + j\frac{\omega}{\gamma J_\mathrm{s}}\alpha - \frac{\omega^2}{\gamma^2 {J_\mathrm{s}}^2(h_0 + N_z + j\,\omega/(\gamma J_\mathrm{s})\,\alpha)} + j\omega\sigma\mu_0 l^2\right)\lambda^2 + j\omega\sigma\mu_0\left(1 + h_0 + j\frac{\omega}{\gamma J_\mathrm{s}}\alpha - \frac{\omega^2}{\gamma^2 {J_\mathrm{s}}^2}\right) = 0, \tag{17}$$

being (17) a biquadratic algebraic equation.

Equation (16) naturally satisfies the boundary condition (10) and (11), but Eqs. (12) and (14) are satisfied only through suitable values of C_1 and C_2 that are obtained by solving the algebraic system

$$\begin{pmatrix} \lambda_1\coth\left(\lambda_1\frac{d}{2}\right) & \lambda_2\coth\left(\lambda_2\frac{d}{2}\right) \\ {\lambda_1}^3\coth\left(\lambda_1\frac{d}{2}\right) & {\lambda_2}^3\coth\left(\lambda_2\frac{d}{2}\right) \end{pmatrix}\cdot\begin{pmatrix} C_1 \\ C_2 \end{pmatrix} = \begin{pmatrix} \omega\sigma B_\mathrm{p}\frac{d}{2} \\ -\omega^2\sigma^2\mu_0 B_\mathrm{p}\frac{d}{2} \end{pmatrix} \tag{18}$$

The applied field is eventually obtained as

$$\underline{h}_a = \underline{h}_y(d/2) = C_1\coth(\lambda_1\, d/2) + C_2\coth(\lambda_2\, d/2). \tag{19}$$

The whole permeability is then computed as

$$\underline{\mu}(j\omega) = \frac{B_\mathrm{p}}{\mu_0\cdot\underline{h}_a}. \tag{20}$$

Finally, the specific rotational loss is computed as

$$W_\mathrm{rot} = \frac{\pi}{\mu_0}\cdot\frac{\mu''}{|\underline{\mu}|^2}\cdot B_\mathrm{p}^2. \tag{21}$$

The reader will find the related software algorithms in [10].

We have applied this theory to the case of the 20.3 μm tick Finemet, endowed with given transverse anisotropy, K_u = ~24 J/m^3, saturation polarization J_s = 1.25 T, conductivity ρ = 118 × 10^{-8} Ω·m. The following parameters have been identified: the static susceptivity χ_DC = 25000, the perpendicular demagnetizing factor N_z = 0.64, the damping factor α = 0.054, the exchange length l = 10.9 nm. The ensuing value of the relaxation frequency is f_1 = 26 MHz, and the resonance frequency is f_0 = 180 MHz. Figure 8 shows the behaviour of the real and imaginary parts of the complex susceptivity vs. frequency.

The theoretical and experimental results are summarized in Fig. 9. Here, the blue-dashed line represents the theoretical (computed) rotational loss. Beyond a few MHz, the experimental and the theoretical curve superpose. The difference between the experimental and the theoretical curves provides the hysteretic and the excess loss. The excess and hysteretic loss reduce to zero beyond a few MHz. In addition, the dashed red curve provides the spin damping loss component. By this theoretical approach, we can compute the rotational loss contribution, and we can separate different loss components upon the whole frequency spectrum. Figures 10 and 11 compare the measured

permeability (symbols) to the theoretical permeability (continuous lines) at two peak inductions.

IV. CONCLUSIONS

The DC – 1 GHz magnetic loss and permeability of nanocrystalline and amorphous ribbons can be theoretically assessed by separating the contributions to the magnetization reversal provided by the domain walls and the rotational process. In the specific case where minimum losses at all frequencies are aimed at, a treatment at moderate temperature (around 300 °C) under transverse saturating magnetic field leads to transverse anisotropy and ensuing transverse domain structure, engendering dominant magnetization process by rotations. This case is especially favorable to excellent response of the material extending deep in the MHz range and to accurate theoretical treatment. This has been demonstrated in this work regarding field-treated Co-based amorphous ribbons and nanocrystalline alloys, where the theoretical approach to the dynamics of the magnetization process by rotation is carried out applying the Maxwell's equation on materials whose magnetic constitutive equation can be identified as a complex permeability, obtained as solution of the appropriate Landau-Lifshitz equation. While demonstrating that in these systems the relaxation phenomena anticipate and overcome the resonance effects, the separate contributions to the energy dissipation by eddy currents and spin damping are worked out. These eventually appear as high-frequency phenomena and, by comparison with the measured losses, we obtain the further dissipation contribution provided by the moving domain walls. Their motion is largely restrained beyond the kHz range, but it provides the whole quasi-static (hysteresis) and low frequency (excess) losses.

REFERENCES

[1] F. Fiorillo, G. Bertotti, C. Appino, M. Pasquale, Soft magnetic materials, in: *Wiley Encyclopaedia of Electrical and Electronics Engineering,* J. G. Webster, Ed. (Wiley, 2016). doi: 10.1002/047134608X.

[2] J.M. Silveira, E. Ferrara, D. Huber, and T.C. Monson, Soft magnetic materials for a sustainable and electrified world, Science **362** (2018) eaao0195. doi: 10.1126/science.aao019.

[3] O. Geoffroy and J.L. Porteseil, Les matériaux doux pour l'électrotechnique et l'électronique basse fréquence, in: *Magnétisme*, E. du Trémolet de Lacheisserie, Ed. (Presses Univ. De Grenoble, 1999), pp. 89-154.

[4] J.C. Peuzin, Les matériaux doux pour l'électronique haute fréquence, in: *Magnétisme*, E. du Trémolet de Lacheisserie, Ed. (Presses Univ. De Grenoble, 1999), pp.155-211.

[5] G. Herzer, Nanocrystalline soft magnetic alloys. in: *Handbook of Magnetic Materials*, K.H.J. Buschow, Ed., Vol.10, Elsevier, Amsterdam, 1997, pp. 415 - 462. doi:10.1016/S1567-2719(97)10007-5.

[6] J. Petzold, Applications of nanocrystalline soft magnetic materials for modern electronic devices, *Scr. Mater*. **48** (2003) 895–901. doi:10.1016/S1359-6462(02)00624-3.

[7] V. Harris, Modern microwave ferrites, *IEEE Trans. Magn*. **48** (2012) pp. 1075-1104. doi: 10.1109/TMAG.2011.2180732.

[8] F. Fiorillo, "Measurements of magnetic materials," *Metrologia* **47** (2010) pp. S114-S142. DOI: 10.1088/0026-1394/47/2/S11.

[9] C. Ragusa, S. Dobák, C. Beatrice, L. Solimene, F. Fiorillo, "(EMPIR 19ENG06 HEFMAG) Data sets of measurements of magnetic loss and complex permeability on amorphous and nanocrystalline samples up to the MHz range". Zenodo, Aug. 28, 2023. doi: 10.5281/zenodo.8292861.

[10] C. Ragusa and L. Solimene, "(EMPIR 19ENG06 HEFMAG) "Loss in Ribbon", a Software for the Computation of Complex Permeability and Losses in Amorphous and Nanocrystalline Magnetic Ribbons". Zenodo, June 29, 2022. doi: 10.5281/zenodo.8299052.

Figures

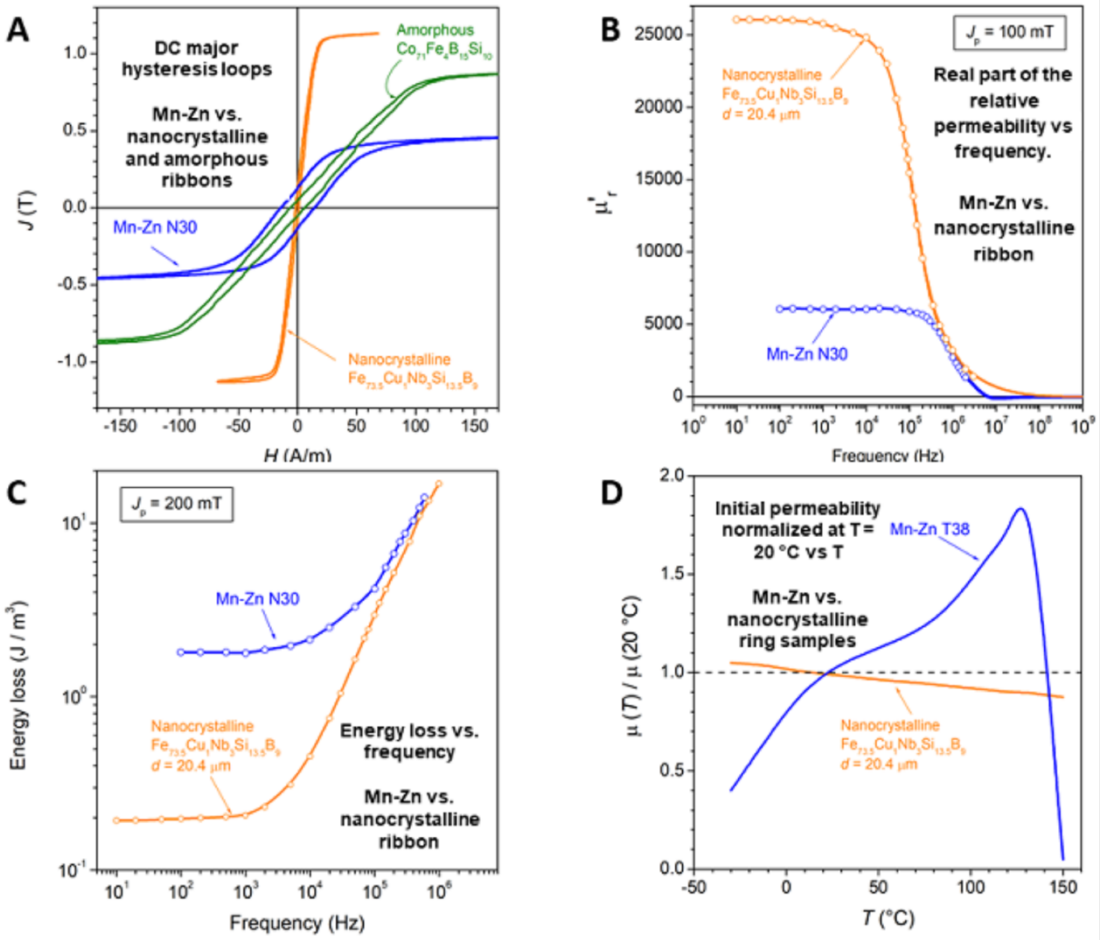

FIGURE 1. Overview of the magnetic behaviour of Finemet and Co-based amorphous ribbons, and Mn-Zn sintered ferrites.

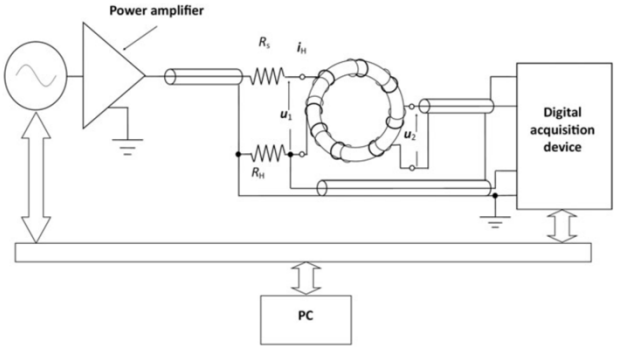

FIGURE 2. An example of a flux-metric setup by which the magnetic properties, the specific power loss, and the amplitude permeability are obtained under different peak inductions and frequencies up to 10 MHz.

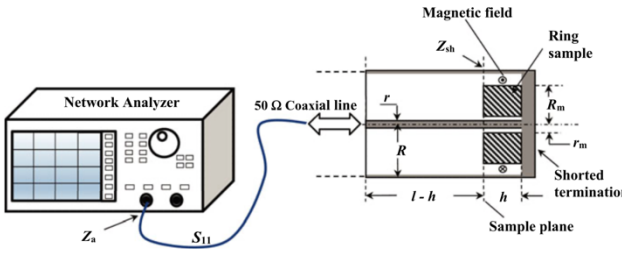

FIGURE 3. The complex permeability of a ring sample is obtained up to a few GHz, using a Vector Network Analyzer (VNA) feeding a shorted 50-ohm coaxial cable, which holds the sample at its bottom. The VNA generates a frequency swept signal and provides the frequency dependence of impedance at the sample plane. The impedance can be related to the geometry of the sample, frequency, and complex permeability of the core that is eventually retrieved.

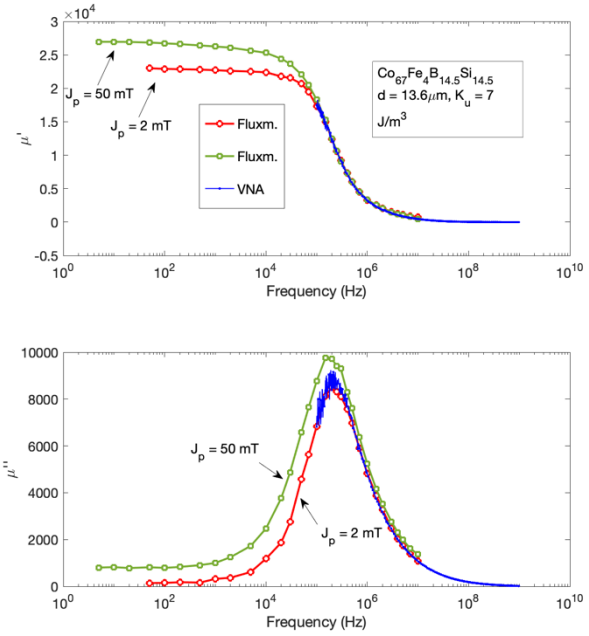

FIGURE 4. Real μ' and imaginary μ'' permeability components versus frequency measured in a ~13 μm tick Co-based amorphous ribbon endowed with transverse anisotropy, K_u = ~7 J/m³. The fluxmetric measurements (symbols) are performed at peak inductions 2 mT and 50 mT up to a few MHz. The transmission line results (continuous line), obtained in the upper frequency range, coincide with the fluxmetric measurements beyond a few hundred kHz. The overlapping region shrinks on increasing peak induction because of a correspondingly increasing proportion of the domain wall processes with respect to the rotations.

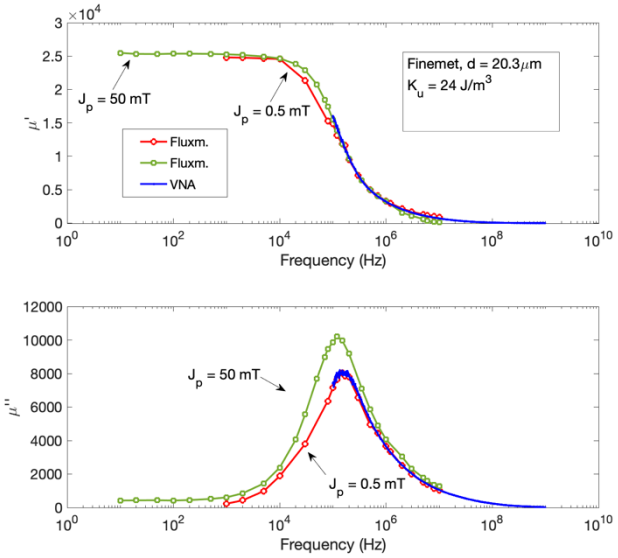

FIGURE 5. Real *μ*' and imaginary *μ*'' permeability components versus frequency measured in in a ~20 *μ*m tick Finemet ribbon endowed with transverse anisotropy, K_u = ~24 J/m³. The fluxmetric measurements (symbols) are performed at peak inductions 0.5 mT and 50 mT up to a few MHz. The transmission line results (continuous line), obtained in the upper frequency range, coincide with the fluxmetric measurements beyond a few hundred kHz. The overlapping region shrinks on increasing peak induction because of a correspondingly increasing proportion of the domain wall processes with respect to the rotations.

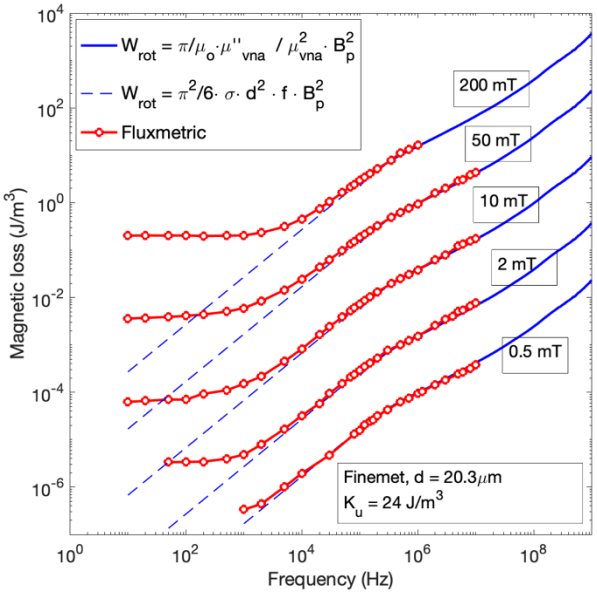

FIGURE 6. Energy loss W(f) versus frequency up to 1 GHz in in a 20 *μ*m tick Finemet ribbons endowed with transverse anisotropy. The loss is directly measured at given peak induction by the fluxmetric method up to 10 MHz (symbols). By the transmission line (TL) method one gets, starting from a few hundred kHz, the real μ′(*f*) and imaginary μ′′(*f*) permeability components. *W(f)* is then calculated for any peak induction by Eq. (1) (continuous lines). The two methods provide matching *W(f)* values in the overlapping frequency interval.

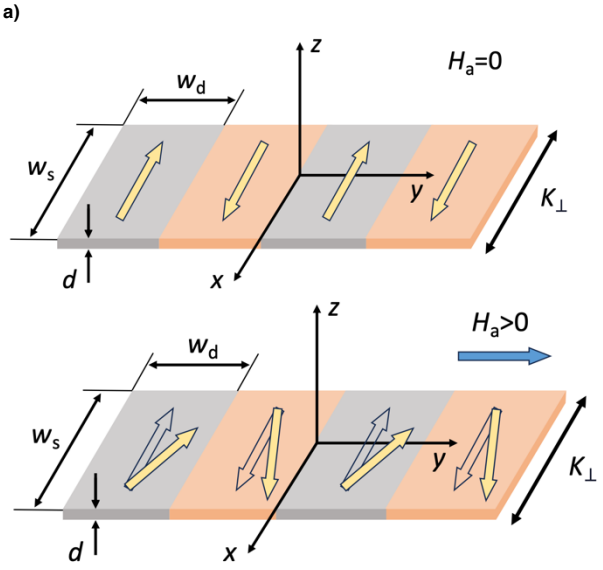

FIGURE 7. The case of transversally field-annealed ribbons, where a sharp transverse domain structure is induced by annealing under saturating transverse field (a) is considered. Under an oscillating longitudinal applied field, the magnetization process will follow almost completely the mechanism of spin rotation (b).

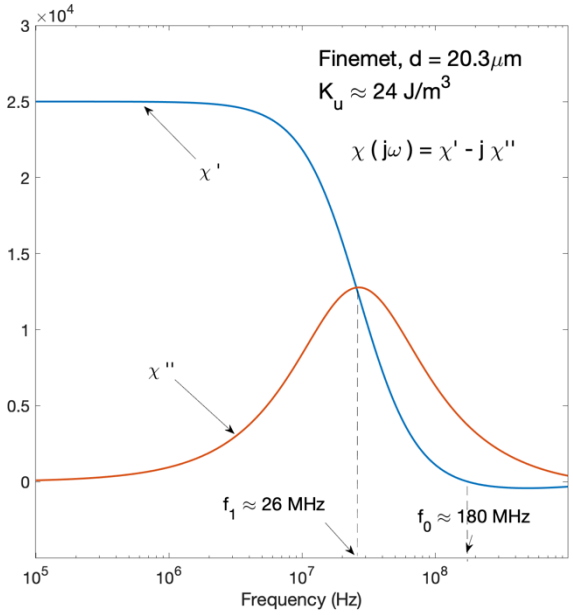

FIGURE 8. Calculated behavior of the complex susceptivity vs. frequency in the case of the 20.3 μm tick Finemet, endowed with given transverse anisotropy, K_u = ~24 J/m^3. The polarization at saturation is J_s = 1.25 T, and the conductivity is $\rho = 118 \times 10^{-8}$ Ω·m. The following parameters have been identified: the static susceptivity χ_{DC} = 25 000, the perpendicular demagnetizing factor N_z = 0.64, the damping factor α = 0.054, and the exchange length l = 10.9 nm. The ensuing value of the relaxation frequency is f_1 = 26 MHz, and the resonance frequency is f_0 = 180 MHz.

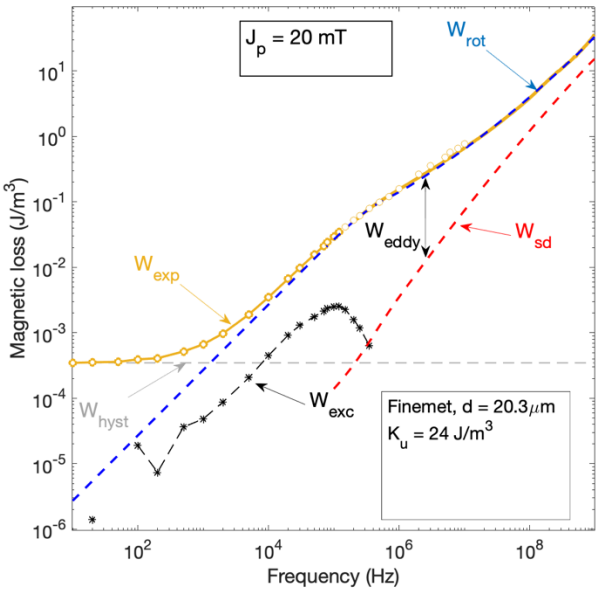

FIGURE 9. Example of energy loss measured up to 1 GHz at J_p = 20 mT in the 20 μm tick, Finemet ribbon endowed with a defined transversal anisotropy (K_u ~ 24 J/m³), and theoretical prediction of the rotational contribution through coupled Landau-Lifshitz-Gilbert and Maxwell's diffusion equations. The blue-dashed line represents the theoretical rotational loss. The difference between the measured and the theoretical loss provides the hysteresis and the excess losses. Beyond a few MHz, the experimental and the theoretical curve superpose and the excess and hysteretic loss reduce to zero. The dashed red curve provides the (theoretical) spin damping loss component W_{sd}. The difference $W_{rot} - W_{sd}$ provides the eddy current loss W_{eddy}.

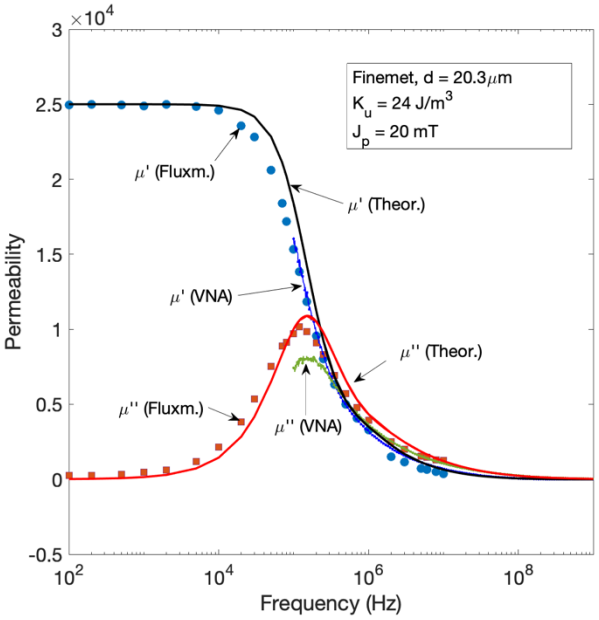

FIGURE 10. Real μ' (blue dots) and imaginary μ'' (red square) permeability vs. frequency measured at peak induction 20 mT in the ~20 μm tick Finemet ribbon endowed with transverse anisotropy, K_u = ~24 J/m³. The theoretical rotational permeability components are represented by continuous lines.

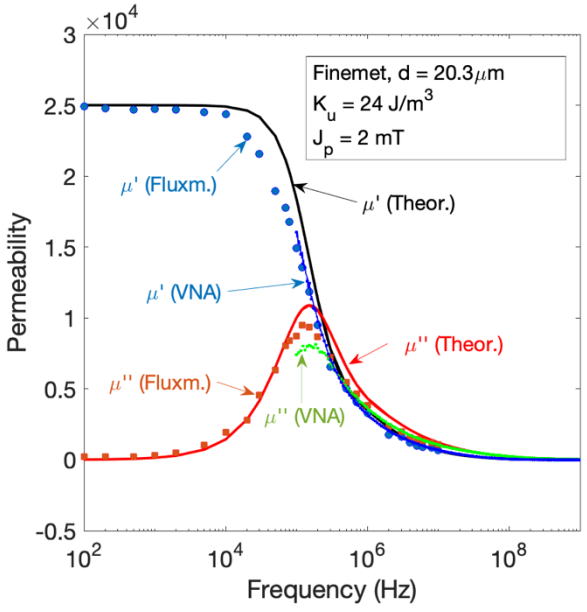

FIGURE 11. Real μ' (blue dots) and imaginary μ'' (red square) permeability vs. frequency measured at peak induction 2 mT in the ~20 μm tick Finemet ribbon endowed with transverse anisotropy, K_u = ~24 J/m³. The theoretical rotational permeability components are represented by continuous lines.